nature communications

Article

https://doi.org/10.1038/s41467-024-51999-y

Delineating the stepwise millisecond allosteric activation mechanism of the class C GPCR dimer mGlu5

Received: 23 September 2023

Accepted: 21 August 2024

Published online: 30 August 2024

Check for updates

Mingyu Li[1,2,4], Xiaobing Lan[2,4], Xinchao Shi[1], Chunhao Zhu[2], Xun Lu[1], Jun Pu[3], Shaoyong Lu[1,2] ✉ & Jian Zhang[1,2] ✉

Two-thirds of signaling hormones and one-third of approved drugs exert their effects by binding and modulating the G protein-coupled receptors (GPCRs) activation. While the activation mechanism for monomeric GPCRs has been well-established, little is known about GPCRs in dimeric form. Here, by combining transition pathway generation, extensive atomistic simulation-based Markov state models, and experimental signaling assays, we reveal an asymmetric, stepwise millisecond allosteric activation mechanism for the metabotropic glutamate receptor subtype 5 receptor (mGlu5), an obligate dimeric class C GPCR. The dynamic picture is presented that agonist binding induces dimeric ectodomains compaction, amplified by the precise association of the cysteine-rich domains, ultimately loosely bringing the intracellular 7-transmembrane (7TM) domains into proximity and establishing an asymmetric TM6-TM6 interface. The active inter-domain interface enhances their intra-domain flexibility, triggering the activation of micro-switches crucial for downstream signal transduction. Furthermore, we show that the positive allosteric modulator stabilizes both the active inter-domain 7TM interface and an open, extended intra-domain ICL2 conformation. This stabilization leads to the formation of a pseudo-cavity composed of the ICL2, ICL3, TM3, and C-terminus, which facilitates G protein coordination. Our strategy may be generalizable for characterizing millisecond events in other allosteric systems.

G protein-coupled receptors (GPCRs) are the largest and most diverse superfamily of transmembrane proteins in eukaryotes. They are crucial transducers that sense a wide range of extracellular stimuli including metabolites, hormones, ions, and photons. These receptors relay these signals to intracellular effectors such as G-proteins and β-arrestins, orchestrating nearly all physiological processes. Hence, they are key targets for drug discovery[1–3]. The sophisticated signals mediated by GPCRs can be precisely integrated within a single cell, primarily achieved through inter-communication among downstream signaling cascades[4]. Additionally, allosteric interactions between receptors, specifically through direct contact with dimeric and/or oligomeric forms, can regulate signaling and subsequent physiological functions[5–8]. However, the details of these allosteric interactions within dimers and/or oligomers remain unclear owing to the considerable magnitude of the assembly of large protein machines and the highly dynamic nature of allostery.

[1]State Key Laboratory of Medical Genomics, National Research Center for Translational Medicine at Shanghai, Medicinal Chemistry and Bioinformatics Center, Ruijin Hospital, Shanghai Jiao Tong University School of Medicine, Shanghai 200025, China. [2]Key Laboratory of Protection, Development and Utilization of Medicinal Resources in Liupanshan Area, Ministry of Education, Peptide & Protein Drug Research Center, School of Pharmacy, Ningxia Medical University, Yinchuan 750004, China. [3]Department of Cardiology, Renji Hospital, Shanghai Jiao Tong University School of Medicine, Shanghai 200120, China. [4]These authors contributed equally: Mingyu Li, Xiaobing Lan. ✉e-mail: lushaoyong@sjtu.edu.cn; jian.zhang@sjtu.edu.cn

https://doi.org/10.1038/s41467-024-51999-y

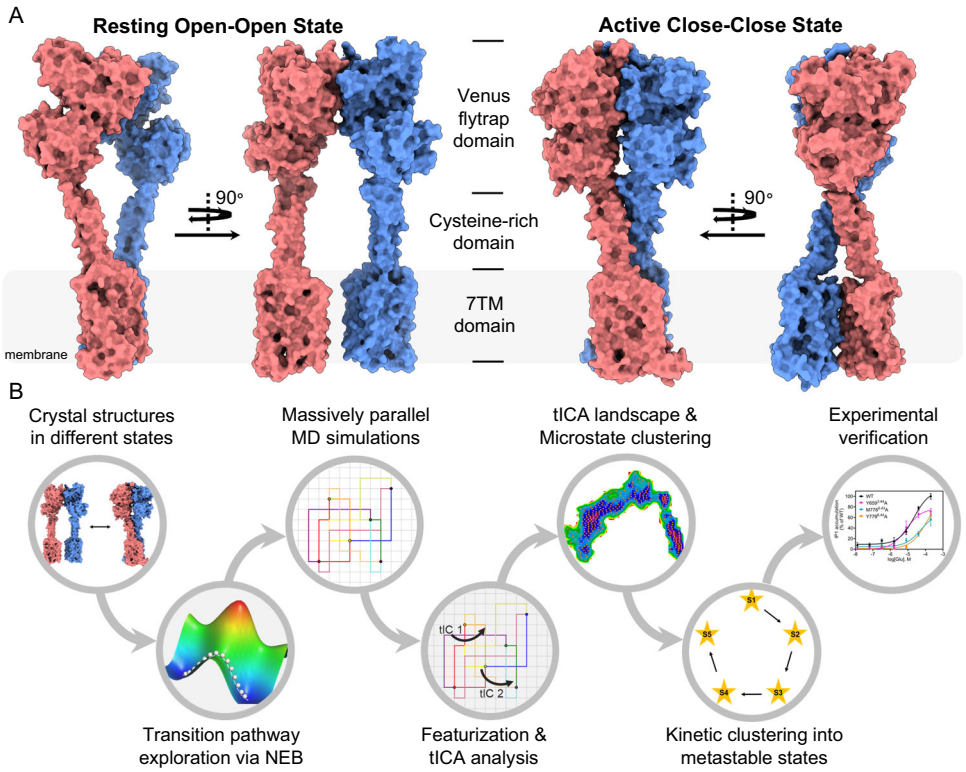

Fig. 1 | Workflow exploring the molecular activation mechanism of mGlu5. **A** Structural overview of resting and active mGlu5 crystal structures. The resting (left; PDB ID 6N52) and active (right; PDB ID 6N51) states of mGlu5 are represented in surface. Three major functional domains, namely, the Venus flytrap, the cysteine-rich, and the 7TM domains are highlighted and labeled in the center. Protomer A is depicted in red, while protomer B is in blue. This color-coding scheme for mGlu5 protomers is used consistently in all figures. All figures depicting structures were drawn by ChimeraX or PyMOL. **B** Schematic overview of the pipeline for investigating mGlu5 activation. Leveraging crystal structures in varying states of interest, we employ NEB simulations for enhanced sampling of system dynamics. Massively parallel unbiased MD simulations are then deployed to capture the fine dynamics of the system. Featurization and tICA allow us to examine the free energy profiles and an MSM model is subsequently established to characterize the system dynamics. These computational findings are finally validated through experiments.

Class C GPCRs, including metabotropic glutamate receptors (mGlu) and gamma-aminobutyric acid B ($GABA_B$) receptors most prominently, serve as optimal models for investigating GPCR direct allosteric interactions due to their obligate dimeric nature[9–11]. Recently, the full-length metabotropic glutamate receptor subtype 5 (mGlu5) homodimer structures, both in the inactive and active conformations, were determined[12] (Fig. 1A). Unlike the conventional structural paradigm observed in class A and B GPCRs, class C GPCRs possess relatively large extracellular domains that feature a bilobed 'clamshell' Venus flytrap (VFT) domain with orthosteric ligand-binding sites and a cysteine-rich domain (CRD) (except for $GABA_B$ receptors) that acts as a semirigid linker connecting the VFT and the seven-helix transmembrane (7TM) domain[13]. In class A and B GPCRs, agonist binding at orthosteric sites induces significant intra-domain residue network reorganization, leading to pronounced outward displacement of TM6 and the opening of the intracellular cavity for downstream effector binding[14–19]. Instead, class C GPCRs undergo a different process in which agonist binding at the clefts of two VFT domains triggers the closure of their lobes. This stabilizes a compact VFT conformation that further propagates conformational rearrangements via CRD linkers to the 7TM domains and brings each 7TM domain into close proximity[20–24]. Notably, each TM6 undergoes minor cytosolic movement and rotation to establish an interacting TM6–TM6 interface[11,18]. Although the cryo-EM mGlu5 structures highlighted notable conformational differences between its inactive and active states, these static snapshots were incapable of elucidating the mechanism underlying the transition between these states. Furthermore, the allosteric mechanism underlying the propagation of the local ligand-induced signal over a remarkable distance of 120 Å to reach the intracellular G-protein-binding site, which involved the coordination of three distinct structural domains (VFT, CRD, and 7TM domains) remains unclear. What intermediates are encountered throughout the activation process? How do the 7TM domains of mGlu5 reorient themselves to establish an active TM6–TM6 interface? How does mGlu5 achieve full activation by coupling with its G protein partner?

Atomistic molecular dynamics (MD) simulations have emerged as powerful tools to tackle these challenges[25,26]. By leveraging a static experimental structure as a starting point, MD simulations can predict the temporal evolution of atom locations guided by Newton's laws and provide a comprehensive view of protein dynamics at the atomic level. Indeed, MD simulations have successfully elucidated the activation mechanisms pertaining to class A and B GPCRs[14,16]. In terms of class C GPCRs, previous studies have focused on simple simulations of the isolated VFT or 7TM domains[27–29] or utilized computationally modeled structures with simulation durations that only spanned several nanoseconds or microseconds (μs)[30–32]. These biased and short MD simulations, however, are inadequate for deciphering large conformational arrangements during the activation of full-length class C GPCRs, capturing comprehensive conformational ensembles, and identifying crucial conformational intermediates along the activation pathway.

To address these intriguing mysteries, we designed a combined computational and experimental framework that couples transition exploration using nudged elastic band (NEB), massively parallel distributed MD simulation-based Markov state model (MSM), and inositol monophosphate (IP1) accumulation assay to disclose the activation conformational landscape of mGlu5 (Fig. 1B). Here, we discover an asymmetric stepwise activation mechanism underlying class C GPCR inter-subunit dimerization, occurring in ~1 ms, alongside intra-subunit

https://doi.org/10.1038/s41467-024-51999-y

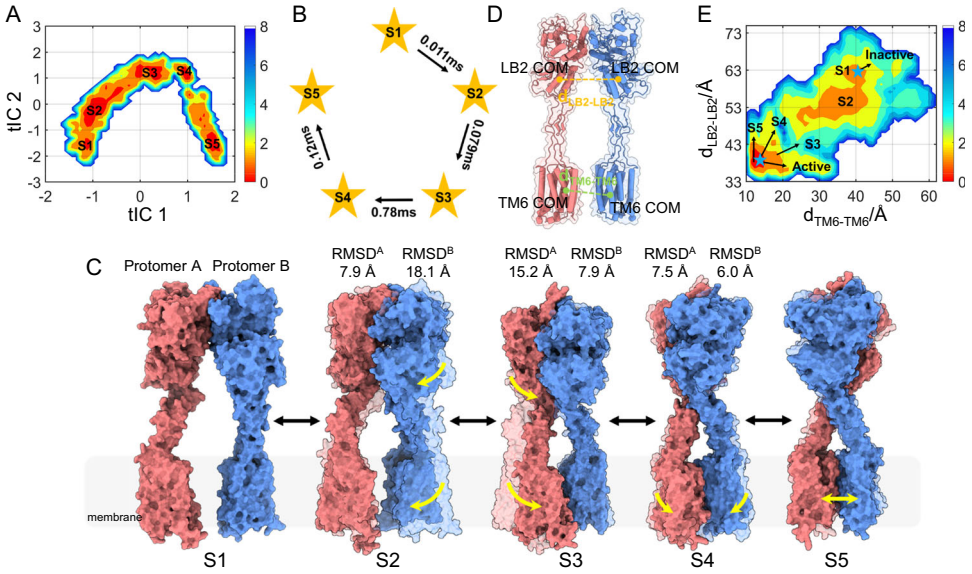

Fig. 2 | A stepwise activation landscape of mGlu5 dimer. A Conformational landscape of mGlu5 derived from the application of the first two components resolved by tICA. Each metastable state is labeled within its corresponding energy basin. The free energy scales of the landscape are shown on the right and are expressed in kcal/mol. **B** The transition time among the five metastable states. **C** Surface representations of the representative structures extracted from the five metastable states. From left to right: the first to fifth structures represent S1 to S5 states. The second to fifth transparent structures represent S1 to S4 states after superimposition. Large yellow arrows in the second and third structures highlight the significant movement of protomers A and B, respectively. Smaller arrows in the fourth and fifth structures indicate slight movement of the two protomers. **D** Two CVs that represent the distances between the VFT domain (calculated by LB2-LB2 COM distance) and 7TM domains (calculated by TM6–TM6 COM distance) are marked on mGlu5. **E** Coarse-grained FEL generated using the CVs in (**D**). Arrows and direct labels highlight different metastable states within the landscape. The blue pentastars at the top and bottom represent the inactive and active cryo-EM structures, respectively.

conformational rearrangements. Five critical metastable conformational states are identified, and the mechanism pertaining to the dynamic G_q coupling process is provided along the full activation pathway. These findings would enhance our understanding of the diverse intermediate states and conformational dynamics underlying dimeric GPCR activation and provide a comprehensive database of mGlu5 conformations to expedite the development of innovative GPCR modulators.

Results

Extensive unbiased MD simulations uncover a stepwise inter-subunit rearrangement and milliseconds timescale during mGlu5 activation

Two full-length crystal structures of mGlu5 were available when we performed this study, with one in the apo state (the "inactive structure," PDB ID: 6N52) and the other in the active conformation bound to a nanobody and a potent agonist (the "active structure," PDB ID: 6N51)[12]. To efficiently disclose the conformational landscape of the mGlu5 inter-subunit activation pathway, we first generated a converge minimum energy path (MEP) that bridges the inactive and active structures by inserting numerous "replicas" interconnected through NEB (Supplementary Note 1 and Supplementary Fig. 1). The nanobody in the active structure was removed, and the two L-quisqualates bound to the VFTs were replaced by their natural agonists, L-glutamates. The glutamates were docked into the inactive structure to imitate the agonist-induced mGlu5 activation in vivo. After a simulated annealing procedure, 13 initial conformations spread over the MEP were selected and subsequently embedded into a 1-palmitoyl-2-oleoyl-sn-glycero-3-phosphocholine (POPC) bilayer membrane, explicit counterions, and water to perform massively parallel MD simulations in an unbiased manner. Each system underwent 1 μs × 10 independent runs with random initial velocities, leading to a cumulative simulation timescale of 130 μs. A comparable simulation protocol has been successfully employed to investigate kinase and GPCR activation mechanisms[33,34].

Based on the MD trajectories, we applied time–structure-based independent component analysis (tICA). This enabled the depiction of the conformational landscape in an objective manner, capturing essential dynamic processes and enhancing its suitability for constructing an MSM[35,36]. A shallow connected free-energy landscape (FEL) was obtained, which exhibited five distinct free-energy basins, each potentially representing a metastable state (Fig. 2A). The convergence of the FEL was proven with varied subsets of the MD samplings, confirming that the sampling has been sufficient to explore the mGlu5 activation (Supplementary Note 2 and Supplementary Fig. 2). To further identify the key intermediate states and determine the activation order and timescale, we constructed an MSM for the mGlu5 system. After identifying the optimal hyperparameters and confirming the convergence of the MSM through the implied timescale test, we applied the robust Perron Cluster Cluster Analysis (PCCA+) algorithm to cluster the conformational ensemble into five MSM metastable states. These states successfully passed the Chapman-Kolmogorov test, indicating that the MSM accurately reproduced the dynamics of the simulation (Supplementary Note 3 and Supplementary Fig. 3). These five-state MSM corresponded well with the observed five-state distribution that was denoted as S1–S5 from left to right in Fig. 2A (we will consistently refer to these states throughout the research). Subsequently, transition path theory (TPT) was utilized to unveil the inter-subunit transition kinetics among the different metastable states. The MSM suggested that the dominant transition pathway followed the sequential order of S1 → S2 → S3 → S4 → S5, with a total timescale of ~1 ms (Fig. 2B).

For a better appreciation of the pivotal mGlu5 conformational states along the transition pathway, we extracted the representative structures of the five metastable states and performed a superimposition analysis (Fig. 2C). A stepwise and asymmetrical structural transformation underlying the activation process was observed. In the first 80 μs period from the S1 to S3, each protomer underwent a sequential conformational arrangement. The overall architecture of

the protomer B initially moved closer to the protomer A (S2 Cα RMSD of 18.1 Å away from S1), whereas the protomer A exhibited relatively minor conformational fluctuations (S2 Cα RMSD of 7.9 Å away from S1). As such, the protomer A (S3 Cα RMSD of 15.2 Å away from S2) approached protomer B (S3 Cα RMSD of 7.9 Å away from S2) during the transition to the S3 state. Once the two protomers were in relative proximity, conformational fluctuations appeared to be attenuated (S4 Cα RMSD of 7.5 Å in protomer A and 6.0 Å in protomer B away from S3). Furthermore, the contacts and relative orientations between the 7TM domains were likely refined in the S4 state. This step was potentially the rate-limiting stage, and it proceeded at ~0.79 ms. Ultimately, further delicate arrangements of inter-subunit interactions occurred during the conformational transition to the S5. Cumulatively, the complete inter-subunit rearrangement between the mGlu5 subunits occurred within ~1 ms, which is consistent with the recently experimentally validated inter-subunit rearrangement timescale of 1–2 ms for the mGlu1 homodimer. Given that mGlu1 shares roughly 70% sequence identity with mGlu5 and the two receptors represent the evolutionary counterparts among the class I mGlu receptors[37], this consistency strongly confirmed the precision and reliability of our computational methodology in capturing the dynamics of mGlu5 activation.

As illustrated in Fig. 2C, the major domain-specific motion observed during activation was compaction between the VFT and 7TM domains. To further substantiate the conformational dynamics of mGlu5, a coarse-grained FEL was constructed by mapping conformational ensembles onto the two collective variables (CVs) that outlined the approaching motion of the VFT and 7TM domains. One variable ($d_{LB2\text{-}LB2}$) was defined as the distance between the center of mass (COM) of the lower lobe 2 (LB2) of each VFT. The other variable ($d_{TM6\text{-}TM6}$) was determined using the distance between the COM points of TM6 (Fig. 2D). The five identified metastable states, together with the two experimentally resolved inactive and active structures, were denoted in the coarse-grained FEL. Indeed, these five metastable states were situated within distinct energy minima in the profiles (Fig. 2E). The S1 and S5, which represent the starting and ending points of the activation process, respectively, as revealed by the tICA and MSM analyses, coincided with the energy minima corresponding to the inactive and active cryo-EM structures. The distance between the VFT and 7TM domains decreased significantly (21.9 Å of VFTs and 20.0 Å of 7TMs) throughout the transition from the S1 to S3. This is consistent with the prominent sequential movement shown in Fig. 2C. During the transition from the S3 to S5, the distances were modified slightly (3.3 Å of VFTs and 5.7 Å of 7TMs), aligning with the refinement of inter-contacts and accommodating minor conformational reorientations. Previous studies have revealed that in the monomeric β_2-adrenergic receptor, the ligand-binding site exhibits loose coupling with the connector site, which, in turn, is loosely coupled to the G protein-binding site[14,38]. Similarly, the divergent coarse-grained FEL indicated that the VFT domains (ligand-binding site) and the 7TM domains (G protein-binding site) were loosely connected. An in-depth examination revealed a loose coupling among the three functionally significant regions of mGlu5—VFT domains, CRDs (connector site), and 7TM domains—appear to be loosely coupled to one another (Supplementary Note 4 and Supplementary Fig. 4). These observations indicated that such loose coupling might serve as a general mechanism for allosteric regulation in both monomeric and dimeric GPCRs.

Collectively, the tICA-based and coarse-grained FEL efficiently elucidated that mGlu5 underwent a stepwise dimer proximity in ~1 ms timescale during the activation pathway in response to glutamate loading.

Activation leads to stepwise compaction of the mGlu5 VFTs

As the agonist-binding site is located between the upper (LB1) and lower (LB2) lobes, the VFT domain is regarded as the starting point of agonist-induced mGlu5 activation. The available crystal structures of VFTs reveal profound conformational changes upon the binding of glutamates or alternative orthosteric agonists[20,39,40]. In terms of inter-domain configuration, the dual VFTs might reorient from a spatially distant (denoted as 'relaxed' or 'R') to an adjacent ('active' or 'A') conformation. Regarding the intra-domain configuration, each VFT exhibits an open conformation (designated as 'o') and is prone to assume a closed conformation ('c') in the absence or presence of orthosteric agonist binding, respectively. Such transition is imperative for downstream effector coupling and signaling.

To investigate the conformational dynamics of the VFT domains, in terms of the inter-domain configuration, $d_{LB2\text{-}LB2}$ was taken as the reaction coordinate. As it decreases, the VFTs transit from the 'R' to 'A' conformation. In terms of the intra-domain configuration, we calculated the summation of Cα RMSD of two VFTs from the crystal VFT conformation in complex with glutamate (PDB ID: 3LMK). This CV (denoted as $RMSD_{VFT}$) quantifies the deviation of the VFTs from the 'c' conformation. The resulting two-dimensional (2D) FEL revealed a shift in the occupation of the main states following glutamates attachment, with the active state assuming dominance (Fig. 3A). The S3–S5 states were situated approximately in the same regions as the Acc VFT state defined in 6N51 with $d_{LB2\text{-}LB2}$ ranging from 37.2–40.5 Å and $RMSD_{VFT}$ from 2.5–3.4 Å. These indicated that the VFT domains indeed underwent significant conformational changes upon glutamates binding. Moreover, in the S3 state, the carboxyl group of glutamates initiated polar interactions with the LB2 of both protomers, inducing a complete closure of the VFTs, with a $RMSD_{VFT}{}^{A}$ value of 1.1 Å and $RMSD_{VFT}{}^{B}$ value of 1.3 Å. In contrast, the VFTs in the S1 state were located in the same free energy minima as the Roo VFT state defined in 6N52 ($d_{LB2\text{-}LB2}$:60.8 to 63.2 Å; $RMSD_{VFT}$:7.3 to 9.0 Å), also exhibiting a Roo conformation. In the S1 state, LB1 primarily anchored to the glutamates, whereas the LB2 interface was not engaged in glutamates binding (Supplementary Note 5 and Supplementary Fig. 5).

Intriguingly, S2 represented an intermediate state along the activation pathway between the Roo and Acc conformations of the VFT domains with $d_{LB2\text{-}LB2}$ and CV_{RMSD} values ranging from 50.0–57.4 Å and 3.7–6.5 Å, respectively. Structural analysis uncovered that the VFTs in the representative S2 conformation adopted a 'co' conformation, wherein the glutamate in the protomer B assumed an unexplored vertical conformation by forming hydrogen bonds with R61 from LB1 and R284, R310, and D312 from LB2; however, no interactions were established with LB2 in the protomer A (Supplementary Note 4 and Supplementary Fig. 4). As a result, the VFT of protomer B exhibited a partial closure ($RMSD_{VFT}{}^{B}$ 1.7 Å), whereas that of protomer A remained open ($RMSD_{VFT}{}^{A}$ 3.2 Å). Considering the relatively minor change in $d_{LB2\text{-}LB2}$ between the intermediate and inactive R states (~8.3 Å) compared with that of the active A state (~14.9 Å), this representative S2 conformation identified by the simulations represents a transient Rco configuration of the VFTs. Such a short-lived Rco state was also observed via single-molecule fluorescence resonance energy transfer (smFRET) experiments on the VFTs of the mGlu2 homodimer and the newly available mGlu2-mGlu3 heterodimer[23,24,41]. An in-depth analysis of the S2 metastable state identified an alternative configuration of the VFTs (denoted as S2′), in which the VFT of the protomer A transited from an open (S2) to a near closed state ($RMSD_{VFT}{}^{A}$ = 1.8 Å), closely approaching a Rcc conformation (Fig. 3B). During the peer-review process, two cryo-EM structures of the mGlu5 in the intermediate-Rcc state with quisqualate bound were determined, providing experimental validation to our mode[42,43]. Moreover, our simulations indicated that the conformational transitions between the Roo and Acc states occurred on a timescale of ~90 μs (Fig. 2B). This timescale is consistent with ~100 μs timescale of the VFT reorientation kinetics observed in all mGlu subtypes, as demonstrated through smFRET studies[44].

The inter-domain conformational arrangements of VFTs in the mGlu receptors are regulated by a conserved hydrophobic interface

https://doi.org/10.1038/s41467-024-51999-y

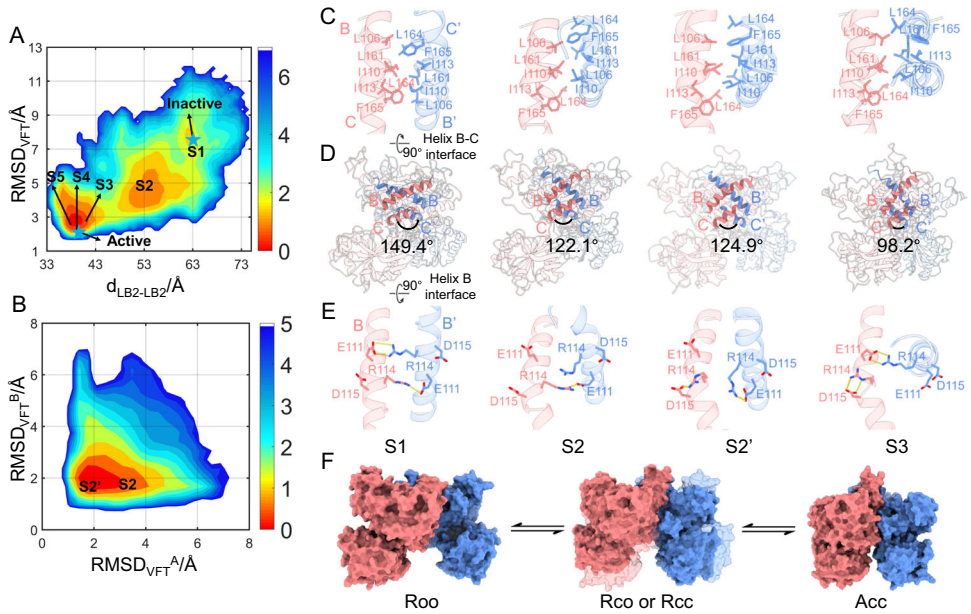

Fig. 3 | Conformational diversity of the VFT domains upon glutamate binding. **A** Activation FEL of VFTs onto the COM of LB2s and Cα RMSD from the conformation of the mGlu5 VFTs crystal structure in complex with glutamate (PDB ID:3LMK). The free energy scales of the landscape are shown on the right and are expressed in kcal/mol. **B** Per-protomer analysis of the S2 metastable state uncovered an alternative configuration of the VFTs, termed S2'. **C** Elevated view of the helix B-C interface from S1 to S3 states. The crucial hydrophobic residues are presented in stick mode. **D** Front view of the helix B-C interface from S1 to S3 states. Both helix B and helix C are highlighted. The helix C cross angle, reflecting the releasement of the hydrophobic constraint of the helix B-C interface, is also labeled. The values are 155.4° and 93.1° in the resting and active cryo-EM structures, respectively. **E** A top view of the helix B-C interface from S1 to S3 states. The helix B is depicted as a cartoon, with key residues shown in stick mode. The crucial polar interactions are represented by yellow dashed lines. **F** Schematic illustration of the activation pathway of VFTs in terms of intra-protomer (open 'o' to close 'c') and inter-protomer (relaxed 'R' to activate 'A') conformational transitions. Upon agonist binding, the co-existence of transient Rco (S2) and Rcc (S2') intermediate conformations was identified between the Roo and Acc conformations.

between the B and C helices at the apical surface of the VFT, which plays a crucial role in agonist-induced structural changes. A study on mGlu2 demonstrated that introducing mutations disrupting this interface increased glutamate affinity and the proportion of the active conformation, even in the absence of glutatmate[45]. The cryo-EM structures of mGlu5 also revealed reorganized interaction networks at the interface between the apo and agonist-bound active conformations[12,43]. Our simulations further supported these findings. In the S1 state, there are tight non-polar interactions between helices B and C (shown in Fig. 3C). These interactions at the interface were gradually attenuated in the following S2, S2' and S3 states, resulting in an increasingly exposed interface. Specifically, in the S2 and S2' state, F165 of the protomer A dissociated from the hydrophobic patch (Fig. 3C), whereas, in the S3, F165 of the other protomer flipped to the opposite side of the interface. The results suggested that agonist binding could release the hydrophobic constraint between the helix B-C interface, as demonstrated by the transitions from the S1 (149.4°) to S2 (122.1°), S2' (124.9°) and then to S3 (98.2°) states, leading to a more compact conformation of the LB2s (Fig. 3D). Aside from non-polar contacts, the disruption of inter-domain and the formation of intra-domain polar interactions at the apical surface of the B helices could further stabilize the active VFT configuration. In the S1 state, inter-domain interactions were maintained between E111 and R114. However, in the following S2 and S3 states, R114 could rotate to form the intra-domain hydrogen bonds with D115 (Fig. 3E).

To summarize the intra- and inter-domain conformational dynamics of the VFTs, our simulations revealed that the VFTs in mGlu5 underwent a series of conformational changes, transitioning between a resting (Roo) state, a transient intermediate (Rco or Rcc) state, and an active (Acc) state on a sub-millisecond timescale (Fig. 3F). These dynamics are driven by the reorganized polar and non-polar interaction networks at the interface between the B and C helices.

Conformational dynamics of CRDs reveal a flexible apical module

The CRD serves as a crucial link between the VFT and 7TM domains in class C GPCRs. It is a semi-rigid structure comprising three antiparallel β-sheets and is highly conserved among all class C GPCRs except for $GABA_B$ receptors. The CRD contains nine cysteine residues. One of these forms an inter-domain disulfide bridge with a cysteine residue in the VFT domain, whereas the others participate in the formation of four intra-domain disulfide bridges. The architecture of the CRD can be subdivided into three submodules, informed by the pattern of cysteine residues as identified in the TNF receptor[46]. The N-terminal apical module (C511 to C534) in the CRD is distinct and lacks resemblance to any established module types. Nevertheless, its structural features are reminiscent of the B module, leading to its denotation as B2' [39]. On the other hand, the middle module (C537–C549) and the C-terminal module (C552–C565) are both categorized within the A1 module (Fig. 4A).

Analysis of the intra-domain mobility of CRD and conformational changes revealed distinct dynamics in different modules. The B2' module in both protomers exhibited higher fluctuations than that of the A1 modules (Supplementary Note 6 and Supplementary Fig. 6). Further cluster analysis based on K-means algorithm was performed to investigate the conformational changes of the B2' module, leading to the identification of five main populations. As shown in Fig. 4a1–a3, the B2' module underwent gradual sideways rotation. Figure 4a4 and a5 revealed that the spatial arrangements of the B2' and the first A1 module were altered, with the first A1 module extending outward. These findings suggested that the CRD can utilize two distinct mechanisms to orient its conformations and interact with the adjacent protomer: One involves a lateral rotation of the B2' muddle, and the other is characterized by the extension of the first A1 module.

https://doi.org/10.1038/s41467-024-51999-y

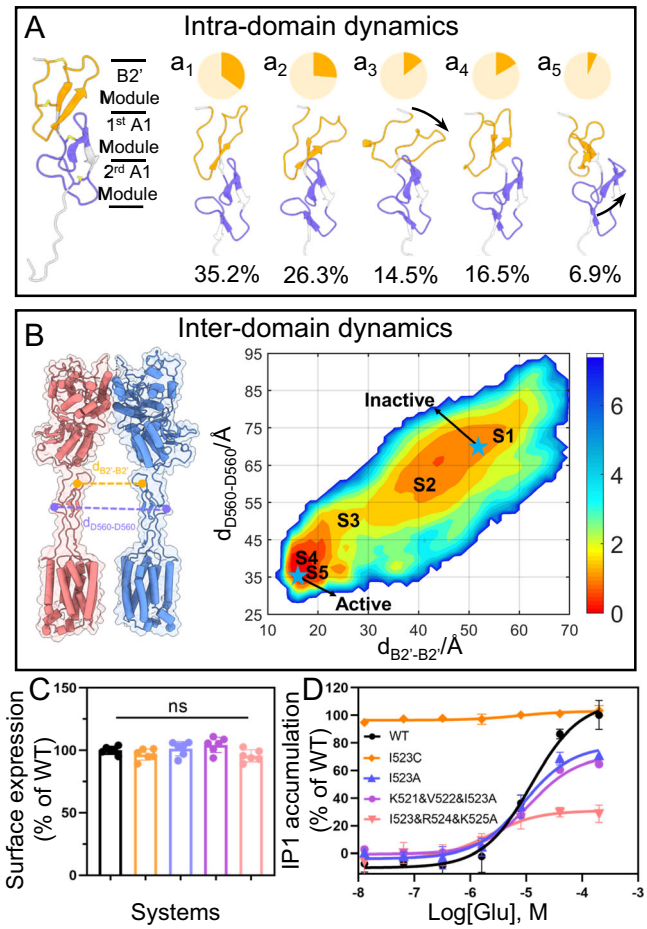

Fig. 4 | CRD association dynamics along mGlu5 activation. A Architecture of three CRD modules. The B2′ module is colored in orange and the two A1 modules are rendered in purple. Four intradomain disulfide bridges are emphasized using stick models. a1–a5 represent five representative intra-domain CRD conformations during simulations; their relative occupations are illustrated in a pie chart above and the specific numbers are presented at the bottom. The two arrows indicate two distinct mechanisms that influence the orientations of the CRD. **B** CVs denote the distances between the near-VFT part of the CRD (B2′-B2′ COM distance) and the near-7TM part (D560-D560 Cα distance) labeled on mGlu5. A free energy profile of CRD inter-domain dynamics is then calculated using the CVs. The free energy scales of the landscape are shown on the right and are expressed in kcal/mol. **C** Quantification of cell surface expression. The bars indicate the mean ± SEM values from six independent experiments. ns, not statistically significant (one-way ANOVA with Dunnett's post hoc test). **D** Crosslinking at the potential surface of the B2′ module by an I523C mutant displays high constitutive activity, as measured using IP accumulation. Alanine mutation of critical residues involved in forming the observed B2′-mediated interface blunt glutamate-induced signaling compared to the WT. Data were from three independent experiments. The bars indicate the mean ± SEM values.

Next, to investigate the inter-domain conformational arrangement of the CRDs, we introduced two CVs, namely, $d_{B2'\text{-}B2'}$, which reflects the spacing between the B2′ modules, and $d_{D560\text{-}D560}$, which signifies the distance between the second A1 modules. Utilizing these CVs, the conformational landscape of CRDs was delineated within a 2D space (Fig. 4B). Concentrating on the dominant population zones (under 2 kcal/mol), the inter-domain arrangement of CRDs can be divided into three steps: Firstly, from the S1 to just before entering the S3 state, the closure of each VFT yielded a substantial progressive reduction in the two CVs that were broadly linearly correlating (Supplementary Fig. 7). The $d_{B2'\text{-}B2'}$ value decreased from 61.6 to 29.2 Å and the $d_{D560\text{-}D560}$ value decreased from 81.0 to 51.6 Å. Next, along with the transient transition of the S3 state, the $d_{B2'\text{-}B2'}$ exhibited a significant decrease (~7.8 Å, from 29.2 to 21.4 Å), whereas $d_{D560\text{-}D560}$ showed a modest reduction (~2.1 Å, from 51.6 to 49.5 Å). This change may be attributed to the pronounced flexibility of the B2′ module, which underwent lateral rotation and initiated the "active" CRDs interface mediated by B2′ module (Supplementary Figs. 7 and 8). Finally, from the end of the S3 to S5 states, $d_{D560\text{-}D560}$ gradually decreased (~15.8 Å, from 49.5 to 33.7 Å) while interactions between B2′ modules underwent subtle adjustment (~3.6 Å, from 21.4 to 17.8 Å).

Importantly, the role of the B2′ module in mediating the active CRDs interface was confirmed by introducing a cysteine-mediated crosslink at the potential interface of the B2′ module (I523C). The I523C mutant maintained comparable levels of cell surface expression but demonstrated a robust constitutive activity as high as the glutamate-induced activity in the wild type (WT) (Fig. 4C, D). Mutating the I523 residue to alanine or altering its adjacent two residues led to the absence of constitutive activity and a significant reduction in efficacy (Fig. 4D and Supplementary Table 3), yet cell surface expression levels remained similar to those of the WT. Such inter-domain dynamics of the CRDs well explained why smFRET studies on mGlu2, mGlu3, and mGlu5 have observed that the CRDs interconvert multiple states through monitoring distance changes between donor and acceptor fluorophores at the position of D548 in mGlu2 and D560 in mGlu5[24,43] (Supplementary Fig. 9).

Taken together, our findings elucidate the dual role of the B2′ module. On the one hand, it is pivotal in maintaining the spatial alignment between the VFTs and CRDs mainly via an inter-domain disulfide bond. On the other hand, the significant mobility of the B2′ module allows it to act as a structural "pioneer", adept at receiving, amplifying, and forwarding signals from the VFT domains through the CRDs and onwards to the 7TM domains. This capacity of the B2′ module underscores its indispensable role in orchestrating complex conformational changes and signal propagation within the receptor, which is consistent with its unique structural singularity within class C GPCRs.

Dynamic allostery in the 7TM domain

Agonist-induced conformational changes ultimately propagate to the intracellular G protein-coupling site of the 7TM domain. A plethora of Cryo-EM structures and dynamic ensembles underscore the common hallmark of G protein coupling in class A and B GPCRs, which is a pronounced outward movement and rotation of TM6 on the cytosolic side that facilitates the deep insertion of G-proteins. Instead, in class C GPCRs, only a subtle TM6 tilt has been identified so far in G_i-stabilized cryo-EM structures, thereby forming a shallow G-protein-binding cavity, indicative of a distinctive overall activation mechanism[18]. During the activation of mGlu5, each 7TM undergoes an inter-domain approach and a 20° rotation upon activation while maintaining an intra-domain that is relatively similar to the apo state ($RMSD_{7TM}$ 4.0 Å, which is the sum of the Cα RMSDs of the 7TMs from the apo conformation)[12]. Consequently, such reorientation engenders a TM6–TM6 interface, appearing to be a hallmark of class C GPCR activation[11,47].

Initially, we investigated whether the intra-domain configuration of 7TM remained rigid throughout activation. Interestingly, it revealed that as the TM6–TM6 interface began to form ($d_{TM6\text{-}TM6}$ < ~20 Å), the 7TM exhibited increased conformational fluctuations ranging from 4.0 to 6.8 Å (Fig. 5A). Further analysis of the per-residue RMSD demonstrated that this increased flexibility was not localized to a specific region of 7TM but rather affected its overall configuration (Supplementary Fig. 10). These findings imply that mGlu5 dimerization at the TM6 interface seems to enhance the flexibility of the overall 7TM domain, thereby eliciting allosteric effects at the G protein-binding site. Such flexibility-driven allosteric effects (also denoted as "dynamic allostery") have been recently recognized as crucial mechanisms for

https://doi.org/10.1038/s41467-024-51999-y

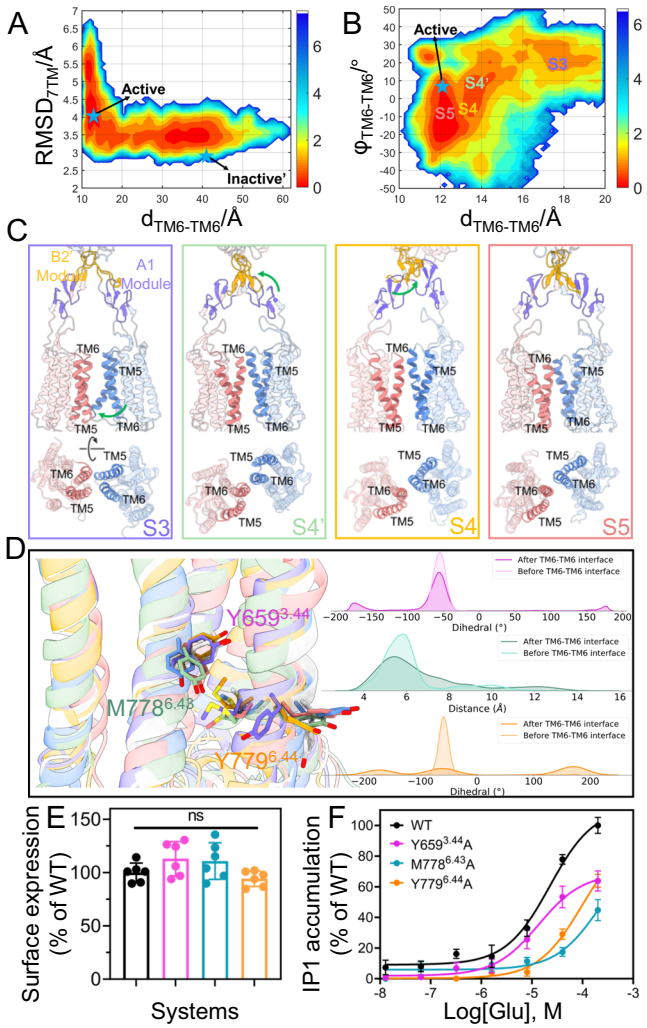

Fig. 5 | Macro-reorientation and micro-switches dynamics at the 7TM interface triggering mGlu5 activation. A Conformation landscape projected onto $d_{TM6\text{-}TM6}$ and Cα RMSD from the inactive mGlu5 cryo-EM structure of the 7TM. After multiple rounds of minimization and equilibration, the well-equilibrated inactive conformation (labeled inactive') shows slight fluctuations from the inactive cryo-EM structure and is depicted as a pentastar. While the active cryo-EM structure is directly represented on the landscape as a pentastar. The free energy scales of the landscape are shown on the right and are expressed in kcal/mol. **B** Conformation landscape projected onto $d_{TM6\text{-}TM6}$ and the dihedral calculated by the Cα atoms of E770$^{6.35A}$, S795$^{6.60A}$, S795$^{6.60B}$, and E770$^{6.35B}$. The labels point out four metastable states within the landscape: S3 (purple), S4′ (green), S4 (orange), and S5 (red). The active cryo-EM structure is also presented as a blue pentastar. This color scheme has been maintained in subsequent illustrations. **C** Representative structures within the 7TM reorientation process. Each structure is presented in a box-colored corresponding to (**B**). The top half of the box provides a frontal view of mGlu5, while the bottom half provides a top view of the 7TM domain. TM5 and TM6 are highlighted to display their orientation. Significant movement patterns are indicated by green arrows. **D** Micro-switch conformations and dynamics of protomer B. The structure of each metastable state is superimposed to demonstrate the difference in the conformation of key micro-switches (inactive cryo-EM structure is colored in gray), including Y779$^{6.44}$ (orange), M658$^{6.43}$ (green), and Y659$^{3.44}$ (magenta). Their conformational distribution before and after the establishment of the TM6–TM6 interface is displayed on the right. Chi1 dihedral is used to present rotamer changes of Y779$^{6.44}$ and Y659$^{3.44}$, while the distance between the Cα atom of Y659$^{3.44}$ and the Cε atom of M658$^{6.43}$ quantifies the displacement of M658$^{6.43}$. The superscripts refer to the GPCRdb numbering scheme. **E**, **F** Mutation of critical micro-switches significantly reduces glutamate-induced signaling compared to the WT, as measured based on IP accumulation with similar levels of cell surface expression. The bars indicate the mean ± SEM values from six (**E**) and three (**F**) independent experiments. ns, not statistically significant (one-way ANOVA with Dunnett's post hoc test).

protein–protein interactions in class B GPCRs with a likely significant role in class C GPCRs activation[48].

Next, we attempted to elucidate the intricate process of TM6–TM6 interface establishment from an inter-domain perspective and capture the intermediate conformations during the process. A dihedral $\varphi_{TM6\text{-}TM6}$ was calculated by the Cα atoms of E770$^{6.35A}$, S795$^{6.60A}$, S795$^{6.60B}$, and E770$^{6.35B}$ to monitor the conformational orientations of the TM6–TM6 interface. The reliability of $\varphi_{TM6\text{-}TM6}$ was confirmed by observing a rotation of ~20° between the apo (28.2°) and active (8.7°) cryo-EM structures. In conjunction with $d_{TM6\text{-}TM6}$, the conformational landscape of the 7TM orientation was obtained (Supplementary Fig. 11). Focusing on the region where the TM6–TM6 interface begins to form, the S3 to S5 states were located within three predominant free-energy basins (Fig. 5B). In the S3, with the $\varphi_{TM6\text{-}TM6}$ of 25.3°, the B2′ modules of CRDs initiated mutual interactions, while the A1 modules remained separate (Supplementary Fig. 7). Transitioning to the S4, the first A1 module of protomer A assumed the configuration depicted in Fig. 4a4, yielding a $\varphi_{TM6\text{-}TM6}$ of −8.7°. Given that the representative conformation of the S4 metastable state was situated in the lower portion of the basin, further analysis revealed an alternative conformation, S4′, in the upper portion. In this state, the first A1 module of protomer B also adopted the Fig. 4a4 configuration, leading to an intermediate $\varphi_{TM6\text{-}TM6}$ of 9.8° (Fig. 5C). These sequential conformational changes of CRDs in both S4′ and S4 might be amplified through their crucial interactions with ECL2s[12], ultimately triggering a 20° rotation in the 7TM domain during activation. Furthermore, the free-energy basin where S5 is located suggests that the TM6–TM6 orientation seen in 6N51 likely denotes a pre-activation state, supported by the trend towards a −8.7° orientation in S5 and even extending to −20° (Fig. 5B). The negative orientations have been observed in recent experimental findings with G protein-stabilized fully active conformations of class C GPCRs ranging from −2.3° in the mGlu2-G_i complex to −20.6° in the mGlu4-G_i complex (Supplementary Table 4)[41,49,50]. In line with the enhanced flexibility along activation, S3 exhibited an $RMSD_{7TM}$ value of 5.0 Å, with the intracellular half of TM5 exhibiting an asymmetrical upward tilt (Supplementary Fig. 12). This tilt changes the configuration of ICL3, potentially orchestrating the conformational arrangement of the G protein-binding site. Indeed, S4′ showed even greater conformational fluctuations ($RMSD_{7TM}$ 5.9 Å), with the intracellular segment of TM3 in protomer B being symmetrically displaced outward, moving K665$^{3.50B}$ away from E770$^{6.35B}$ (4.1 Å) and R668$^{3.53B}$ away from S614$^{2.35B}$ (8.7 Å). The disrupted 'ionic lock' motifs in the protomer B could engender a potential opening cavity to facilitate one G protein binding[51]. Nevertheless, in the absence of G protein binding, these altered ionic locks might revert, reestablishing the TM6–TM6 interface's equilibrium orientation.

Another significant difference before and after the establishment of the TM6–TM6 interface is the rotamer reorientation of Y779$^{6.44}$. In the apo crystal structures, Y779$^{6.44}$ adopted a *gauche*+ conformation in both protomers[12]. However, upon interface formation in both S5 and the active cryo-EM structure, Y779$^{6.44}$ reoriented to a *trans* conformation, tucking between F776$^{6.41}$ and I783$^{6.48}$ (Fig. 5D and Supplementary Fig. 13). During the TM6–TM6 reorientation process, the asymmetric conformations of Y779$^{6.44A}$ and Y779$^{6.44B}$ were captured as the intermediates S3 and S4′. Remarkably, in S4′, protomer B assumed a *trans* conformation, which correlated with the disrupted salt bridges. Such asymmetric behavior, particularly involving residue Y$^{6.44}$, has also been captured in a recently released structure of PAM-bound mGlu5. Moreover, this phenomenon is not unique to mGlu5 but has also been observed across G protein-bound class C GPCR structures such as mGlu4-G_i and mGlu2-G_i. The abrogation of Y$^{6.44}$ in mGlu2 resulted in a

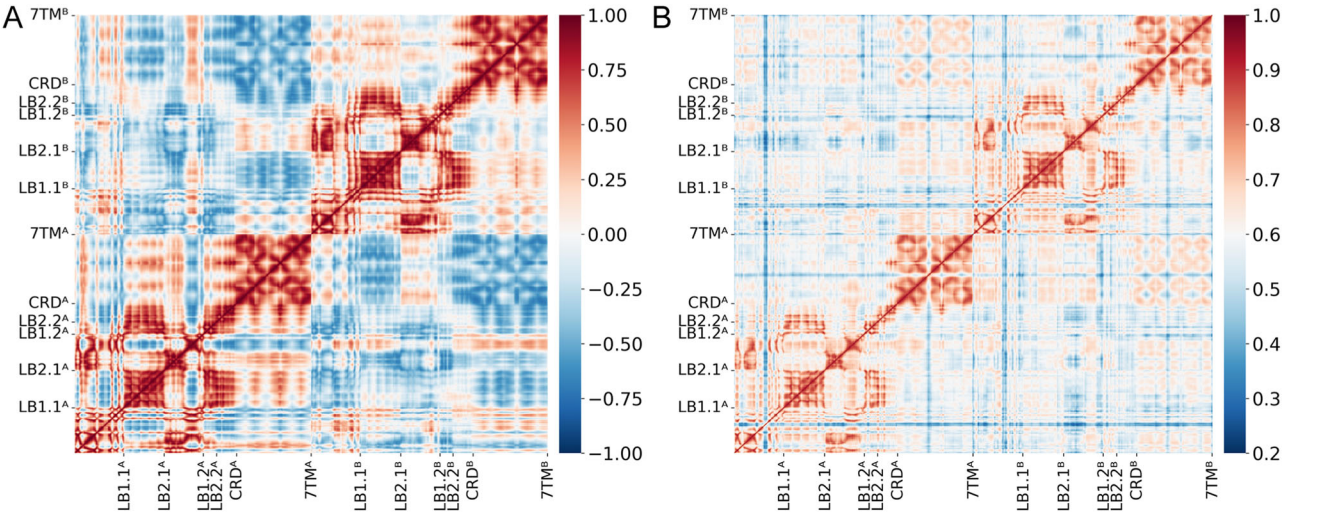

Fig. 6 | Motional correlations among mGlu5 residues during activation. **A** Pairwise Pearson correlation coefficients matrices using the Cα atoms of mGlu5. Regions of positive correlation (depicted in red) represent correlated movements, whereas negative correlation regions (blue) indicate anti-correlated movements. **B** Pairwise mutual information matrices of mGlu5. Only significant correlations, defined by values above 0.2, are displayed.

decrease in the glutamate-stimulated G protein response[49,50]. This asymmetric behavior was also evident in heterodimers involving G proteins, including mGlu2-mGlu3-G_i and mGlu2-mGlu4-G_i (Supplementary Fig. 14)[41]. Our simulations suggested that the rotamer changes of Y779$^{6.44}$ might modify its neighboring residues, particularly M658$^{6.43}$ and Y659$^{3.44}$ (Fig. 5D and Supplementary Fig. 13). Y659$^{3.44}$ is a well-known crucial activation micro-switch in the class A GPCRs and the mGlu receptors, and its conformational changes are essential for the activation process[51–53]. By modifying the side chain of the neighboring residue M658$^{6.43}$, the conformation of Y659$^{3.44}$ may reorient and regulate the activation process. Consistent with this signal transmission pathway, Y779$^{6.44}$, M658$^{6.43}$, and Y659$^{3.44}$ mutations significantly decreased both the potency and efficacy of glutamate-induced activation compared with that in the WT (Fig. 5E, F and Supplementary Table 3). This confirms the importance of these micro-switches in mediating the activation process.

In the aforementioned analysis of the 7TM domains, it was observed that the state of the interaction networks (the intracellular ionic lock motif and asymmetric TM6–TM6 interface) exists in a dynamic equilibrium. This indicated that the conformational shift triggered by glutamate alone might not adequately stabilize its fully active state. This aligned with observations from smFRET and cryo-EM experiments, where the fully active structures of the mGlu receptors have only been identified in the presence of an intracellular effector protein, typically in conjunction with a positive allosteric modulator (PAM)[40,41,49,50,54–56]. To delve deeper into how the PAM and G protein (primarily G_q in mGlu5) impact the dynamics of the receptor and enhance our understanding of mGlu5 full activation, leveraging the recently released cryo-EM structures and Alphafold2-multimer technologies, we conducted unbiased all-atom MD simulations on the two full-length mGlu5 systems: one bound with glutamate and PAM CDPPB (1 μs × 10), and the other with glutamate, PAM, and G_q (1 μs × 10). The results demonstrated that the presence of PAM not only stabilized mGlu5 by tightening the active inter-domain 7TM interface but also maintained the appropriate open and extended intra-domain ICL2 conformation (Supplementary Note 7 and Supplementary Fig. 15). Furthermore, to explore the detailed interaction variations at the mGlu5-7TM-G_q interface in addition to the ICL2, we generated the FEL on the interface contacts via the first two tICs (Supplementary Note 8 and Supplementary Fig. 16). Three metastable states were identified: a pre-coupled G1 state, an intermediate G2 state and a fully activated G3. In the fully activated G3 state, the active-state asymmetric TM6–TM6 interface was formed, with an upward shift in the TM6 of the G_q-coupled protomer facilitating the rearrangement of ICL3. This conformational rearrangement further orchestrated the cytoplasmic tip of TM3, ICL2, and H8 (potentially the C terminus) to envelop the α5 helix of G_q. This G_q binding mode observed in the mGlu5 is entirely distinct from those found in class A GPCRs, providing complementary insights into the full activation mechanism of the dimeric GPCRs.

Long-range allosteric coupling between residues in mGlu5

Allosteric coupling plays a pivotal role in GPCR activation, relying on spatially long-range communication networks both within and between domains[18]. To investigate how agonist binding at the VFT domain transmits signals over a distance of 120 Å to the intracellular G protein-coupling site in the 7TM domain, motion correlation analysis was calculated based on extensive MD simulations. The Pearson correlation map primarily showed linearly correlated motions within protomers, except for LB1 because the LB1s moved apart and the LB1–LB1 interface was disrupted upon glutamates binding (as previously demonstrated) (Fig. 6A). Specifically, after glutamates binding, the LB2 motion displayed a high correlation with the movement of the 7TM domain in the same protomer, suggesting that the glutamate-bound VFT could potentially activate the 7TM domain of the same protomer (denoted as *cis*-activation).

However, given that inter-domain motions often exhibit nonlinear correlations that exceed the descriptive capacity of the Pearson correlation map, we opted for mutual information analysis[57]. Even at separations of 120 Å, significant correlations (>0.6) were observed in the fluctuation of mutual information as a function of pairwise Cα atom distance (Supplementary Fig. 17). In addition to the strong local coupling observed within the VFTs, CRDs, and 7TMs of mGlu5 in the Pearson correlation matrix, closer examination of the mutual information matrix revealed substantial long-range allosteric coupling between the 7TM domain and the VFT, CRD, and 7TM domains of the counterpart protomer (Fig. 6B). This suggests that the glutamate-induced VFT arrangement may also facilitate the activation of the adjacent protomer (denoted as *trans*-activation)[21,58,59].

Discussion

Class C GPCRs are not only quintessential model systems for exploring GPCR dimerization and long-range allosteric activation, extending over 120 Å from the extracellular ligand-binding site to the intracellular effector-binding site, but also valuable therapeutic targets for treating

neural system disorders[60–62]. A comprehensive understanding of the dimerization and allosteric activation landscape is essential for the rational design of therapeutic drugs aimed at modulating class C GPCR signaling in desired ways. In this study, we utilized a graded computational strategy progressing from two distinct structural endpoints through a minimum energy transition pathway (NEB without predefined collective variables) to an extensive FEL (large-scale distributed MD simulations-based MSM). This strategy enabled us to reconstruct the millisecond-scale dimerization and long-range allosteric activation of mGlu5 at the atomic level, from the inactive, agonist-free state to the fully active state through five intermediates. It significantly enhances the efficiency of simulation time compared to traditional brute-force simulations spanning several milliseconds. Most importantly, the adaptability of this strategy, especially without a curated definition of collective variables, suggests its potential applicability in characterizing millisecond-long events in other allosteric systems.

Long timescale simulation of mGlu5 unveiled detailed atomic-level insights into the activation mechanisms of dimeric class C GPCRs (Fig. 7). Initially, upon agonist loading, we observed the co-existence of transient Rco (S2) and Rcc (S2′) conformations, accompanied by a sequential closing of VFTs. Unlike previously established classic binding modes in the active state, glutamate exhibited dynamic binding positions in these intermediate states, indicating substantial flexibility within the VFT domains. During the peer-review process, a transient Rcc state with non-classic binding pose of quisqualate (a glutamate analog) was identified through cryo-EM experiments, lending experimental support to our computational model[42]. Subsequently, the activation signals from VFTs seemed to be amplified by the crucial apical modules (B2′ modules) of the CRDs. The B2′ module not only engages laterally with the neighboring B2′ module—amplifying the signal for the TM6–TM6 interface formation (S3)—but also interacts with the extended A1 module of the adjacent protomer, further modifying the TM6–TM6 interface orientation (S4′ and S4). The simulations underscore the highly flexible nature of CRDs, a trait potentially common across all mGlu receptors[24]. This flexibility enables the precise association of CRDs, which is sufficient for full mGlu activation, confirmed by a robust constitutive activity after the introduction of a cysteine-mediated crosslink at the potential surface of the B2′ module (I523C).

Meanwhile, from S3 to S4, dynamic allostery played an underemphasized role in conjunction with dimerization. As the "active" TM6–TM6 interface formed asymmetrically and underwent negative reorientation, the flexibility of the 7TM significantly increased, facilitating the reorganization of conserved motifs and residue networks within the 7TM domain. Dynamic allostery has also been identified as a regulatory mechanism in class B GPCRs, suggesting that it may be a ubiquitous regulatory mechanism in GPCR signaling[48]. However, this active TM6–TM6 interface appeared not to be sufficiently stabilized by the orthosteric agonist alone, as indicated by its orientation equilibrium in the S5. On the contrary, the addition of a PAM stabilized the inter-domain active TM6–TM6 interface, shifting the intra-domain ICL2 conformation from the inactive closed or collapsed states, which impeded Gq protein binding, to the active open and extended state. Indeed, the involvement of ICL2 was validated by our pioneering effort to illustrate the dynamic interaction variations at the mGlu5-7TM-G_q

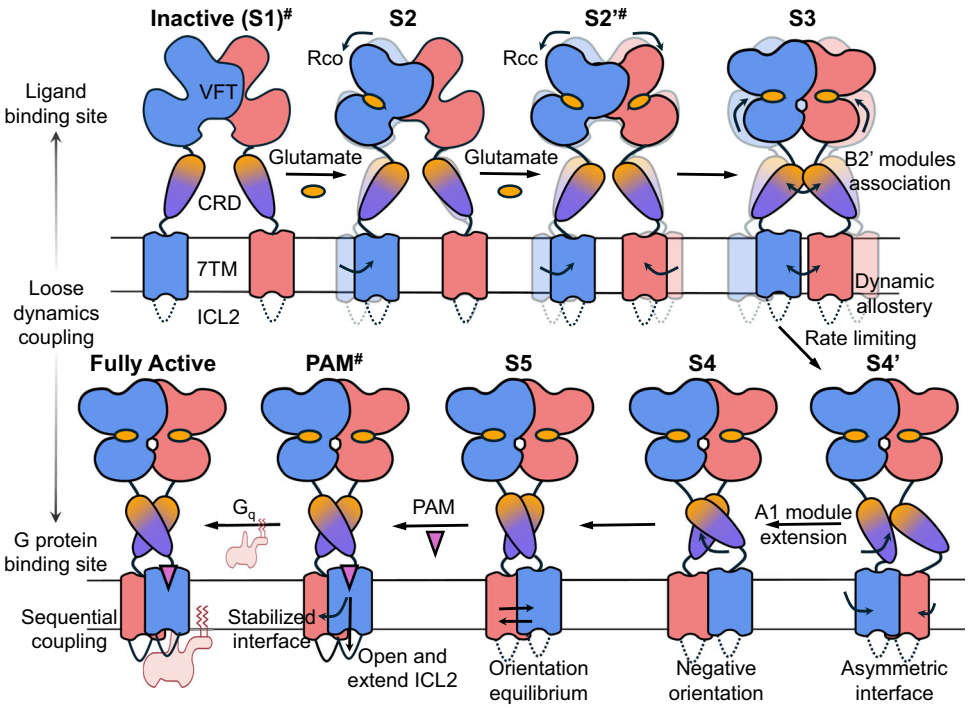

Fig. 7 | Schematic of the asymmetric stepwise allosteric activation model for mGlu5. The stepwise model for the allosteric activation mechanism of mGlu5, illustrating the conformational transitions from the inactive apo state through six intermediate states bound by agonist, to the agonist- and PAM-bound active state, and finally to the Gq-coupled fully active state, with a full-length view in schematic representation. Initially, in the absence of an orthosteric agonist (e.g., glutamate), mGlu5 resides in the apo inactive state (S1). The introduction of orthosteric agonist initiates its sequential binding (S2 and S2′), loosely triggering the conformational rearrangements within the 7TM domains. The closure of both VFTs further brings the protomers into proximity, leading to the initial association of CRDs through the B2′ module. Next, the two A1 modules extend outward (S4′ and S4), their action magnified by crucial interactions with ECL2, forming an asymmetric and negatively oriented "active" TM6–TM6 interface. This active interface may not be sufficiently stabilized by the orthosteric agonist alone, leading to a reversion to the equilibrium orientation of the TM6–TM6 interface (S5). In contrast, the addition of a PAM stabilizes the active TM6–TM6 interface, modulating the ICL2 conformation to an open and extended state (from dash to solid representation). Further coupling of a G_q protein results in a unique fully active conformation (Fully active), facilitating the transduction of intracellular signals. The # superscript represents a conformational state confirmed through both cryo-EM experiments and MD simulations.

interface. Besides the conformational arrangement of ICL2, in the unique fully active state, the cytoplasmic tip of TM3, ICL3 and the H8 (potentially the C terminus) were also engaged to facilitate G protein binding. Unlike class A and B GPCRs, which displace the cytosolic part of the TM6 helix to accommodate G proteins, the class C GPCRs potentially utilize an alternative strategy by forming a pseudo-cavity between the TM3, ICL2, ICL3 and the receptor's C-terminus to coordinate G proteins.

Collectively, our study not only provides a detailed and comprehensive understanding of the molecular machinery, intermediate states, and conformational dynamics underlying class C GPCR activation, but also offers a valuable repository of mGlu5 conformations, which can facilitate the development of innovative modulators for the mGlu receptors. While we achieved success in unraveling the atomic-level mechanistic details of glutamate-induced full activation of dimeric mGlu5, the physiological effects of the identified non-classic glutamate binding poses remain an interesting question to address in future studies. The understanding of the fully activated conformation, particularly regarding the entire ternary complex of the G_q protein, is still in the initial stages of exploration. In addition, future studies are needed to comprehensively investigate the entire activation landscape of all class C GPCR subtypes.

Methods

MD simulation systems preparation

We initially downloaded the apo (PDB ID: 6N52) alongside the orthosteric analog L-quisqualate and nanobody Nb43 bound active mGlu5 (PDB ID: 6N51) crystal structures from the Protein Data Bank (PDB) as the endpoint conformations of the activation pathway with the former inactive conformation serving as the starting structure and the latter active conformation as the ending structure[12]. Both the nanobody and orthosteric analogs were removed from the 6N51. Full-length mGlu5 residues (R25-N832) were included in the simulation. The missing residues in both structures were modeled using the MODELLER software[63] by alignment to the WT human mGlu5 sequence extracted from the UniProt website (UniProt ID: P41594). To explore the mGlu5 activation pathway upon endogenous binding, we, on one hand, utilized Glide[64], implemented in Schrodinger software Suite with the default parameters, to dock the glutamate into the two orthosteric binding sites of 6N51. On the other hand, we aligned the glutamate from the VFT crystals complexed with the glutamate of mGlu5 (PDB ID:3LMK) to guarantee the appropriate Glu-binding pose. The hydrogens were added, and the termini were capped with acetyl and methylamide groups. Subsequently, employing Amber ff14SB force field parameters[65] within the Leap module[66], both structures were solvated in a 10 Å truncated cube with transferable intermolecular potential three-point (TIP3P) waters[67]. The counterions K^+ or Cl^- and an additional 150 mM KCl were also solvated within the systems. Two rounds of energy minimization were performed for both systems to relax the systems thoroughly for the next NEB-enhanced sampling (detailed in the subsequent section). First, we conducted 25,000 steepest descent and 25,000 conjugate gradient energy minimization cycles for all atoms with constraints on TIP3P water molecules and K^+/Cl^- counterions. Subsequently, the same minimization cycles were carried out without any constraints.

Transition pathway exploration via NEB approach

To probe the mGlu5 inter-subunit activation mechanism, we used a powerful NEB approach to identify saddle points and the minimum energy path (MEP) between the two states[68,69]. NEB algorithm does not require the definition of collective variables; instead, it maps the transition pathway within the full Cartesian space. In our study, we initially imagined the pathway from the inactive mGlu5 structure 6N52 to the active 6N51 as an elastic band. This "band" was discretized into a series of "images" (snapshots of the mGlu5 with different conformation along the transition), connected by virtual springs imparting elastic properties and ensuring even distribution along the activation pathway. The endpoints of the band remained fixed, whereas the rest of the band was either allowed to relax in the direction perpendicular to the path or be "nudged" in the direction that decreased the energy of the system. Consequently, this band was identified as the MEP for mGlu5 activation.

Mathematically, the total force on the replica i, $\boldsymbol{F_i}$, can be orthogonally decomposed into parallel ($\boldsymbol{F_i^{//}}$) and perpendicular ($\boldsymbol{F_i^{\perp}}$) components, as shown in Eq. (1).

$$\boldsymbol{F_i} = \boldsymbol{F_i^{//}} + \boldsymbol{F_i^{\perp}} \tag{1}$$

Given all the N atoms in each replica, we computed $\boldsymbol{R_i}$ and $\boldsymbol{\tau}$, which are the 3N-dimensional coordinate vector of replica i and 3N-dimensional tangent unit vector along the MEP, respectively. Thereafter, the parallel and perpendicular forces were determined as follows:

$$\boldsymbol{F_i^{//}} = \left[k_{i+1}(\boldsymbol{R_{i+1}} - \boldsymbol{R_i}) - k_i(\boldsymbol{R_i} - \boldsymbol{R_{i-1}})\cdot\boldsymbol{\tau}\right]\boldsymbol{\tau} \tag{2}$$

$$\boldsymbol{F_i^{\perp}} = -\nabla V(\boldsymbol{R_i}) + (\nabla V(\boldsymbol{R_i})\cdot\boldsymbol{\tau})\boldsymbol{\tau} \tag{3}$$

Here, k_i indicates the spring constant between replica $\boldsymbol{R_i}$ and $\boldsymbol{R_{i+1}}$, and $\nabla V(\boldsymbol{R_i})$ indicates the potential energy gradient with respect to the coordinate vector in the entire system of replica i.

After preparation, a partial NEB (the term partial implies applying NEB to a system subset) procedure available in Amber 20 was used to generate 32 interpolated images between the inactive and active mGlu5 conformations[70]. This procedure allows for the efficient application of NEB in explicitly solvated systems by excluding the solvent atoms. More specifically, the first heating process gradually increased the temperature of the system from 0 to 300 K at a timestep of 0.5 fs using a spring force of 1 kcal/mol/Å and a Langevin collision of 1 ns^{-1}. During subsequent equilibration, annealing, and cooling runs, we employed spring forces of 1, 20, and 20 kcal/mol/Å and Langevin collision frequencies of 100, 75, and 75 ns^{-1}, respectively. In total, the annealing process lasted 7.4 ns, and the systems were initially heated to 500 K, then cooled, and equilibrated at 0 K in intervals of 0.2 ns with a timestep of 0.5 fs. Finally, the images underwent a cooling phase at 0 K for 2 ns with a time step of 1 fs.

MD simulation details

After generating 32 replicates by NEB, we noticed that some conformations were highly similar, which could lead to redundant computational costs in subsequent extensive MD simulations. To alleviate this issue, we calculated the RMSDs between all adjacent replicates. The 13 distinct conformations, including the start and end points, were selected. To further delineate the full activation pathway of the mGlu5, two additional systems were prepared: one with glutamate and CDPPB bound, and another including the binding of glutamate, CDPPB, and the G_q protein.

All 15 systems were initially oriented in the Orientations of Proteins in Membranes server[71]. Subsequently, using the CHARMM-GUI server[72], these structures were embedded in a pre-equilibrated and commonly used POPC lipid membrane[16,17,73]. A pure POPC membrane may have impacted our activation kinetics. During this process, TIP3P water molecules were added up to a distance of 10 Å from the top and bottom of each structure and 150 mM K^+ or Cl^- counterions were solvated and arranged using a Monte Carlo algorithm. The topology and coordinate files in Amber format were obtained by an in-house converter package in CHARMM-GUI (Supplementary Table 1).

For each system, two rounds of energy minimization were conducted to alleviate any inappropriate close interactions. Both rounds

consisted of 25,000 energy-minimization steps of the steepest descent, followed by 25,000 steps of the conjugate gradient. In the first round, all atoms except the lipid, solvent, and counterions were restrained with a force constant of 500 kcal/mol/Å. In the second round of energy minimization, no constraints were applied. Next, the systems were heated from 0 K to 300 K over 300 ps under canonical ensemble (NVT) conditions with a positional restraint of 10 kcal/mol/Å applied to the protein atoms. This was followed by equilibration for 10 ns with a positional restraint of 5 kcal/mol/Å on the protein atoms and 0.5 ns without any restraint under isothermal isobaric (NPT) conditions (300 K, 1 bar). Finally, we performed 10 independent rounds of 1 μs production runs for each of the 15 systems under NPT conditions, which yielded a total simulation timescale of 150 μs. Throughout these simulations, the particle mesh Ewald (PME) method was used for long-range electrostatic interactions, while a cutoff distance of 10 Å was applied for short-range electrostatic and van der Waals interactions[74]. In addition, the SHAKE algorithm was used to constrain covalent bonds involving hydrogen atoms[75]. Snapshots of the simulations were recorded every 100 ps for subsequent analyses.

MSM construction

To maximize the kinetic variance within the features, we evaluated nineteen different feature types with the variational approach for Markov processes (VAMP2) score[76]. The aligned Cα cartesian coordinates of mGlu5 produced the highest mean VAMP2 score across various lag times, making this feature type justified for tICA projection and MSM construction. The high-dimensional vector space was dimensionally reduced using tICA with a lag time of 10 ns.

Through the generalized matrix Rayleigh quotient (GMRQ) score validation and the implied timescale test, The reliability of the MSM was confirmed with the 2 slowest tICs, 300 microstates and a lag time of 10 ns. Then, the 300 microstates were further clustered into 5 macrostates through the PCCA+ algorithm. The 5 macrostates were well separated on the tICA landscape and validated by the Chapman-Kolmogorov test[77]. Overall, we used the MDTraj[78] to compute different feature types, MSMBuilder[79] for parameter optimization, and pyEMMA[80] for scoring the features, performing tICA projection, establishing the MSM and extracting the macrostates.

Subsequently, we applied transition path theory (TPT) to quantify the mean first passage time (MFPT)[81]. The MFPT represents the average time required for a transition from one macrostate to the other macrostate in the MSM. To capture the most representative structure of each metastable state, we first integrated structures close to the center of the macrostates into a smaller trajectory using the MDTraj package[82]. Based on the new trajectories, we selected the representative snapshot of each macrostate according to the pairwise similarity score S_{ij}:

$$S_{ij} = e^{-\frac{d_{ij}}{d_{scale}}} \quad (4)$$

Here, d_{ij} is the RMSD between snapshots i and j, and d_{scale} indicates the standard deviation of d. The snapshot with the highest similarity score was chosen as the most representative structure of each macrostate.

Plasmids and transfection

Human *GRM5* was cloned into a modified pcDNA3.1 (+) vector with a HiBiT tag (Promega) at the N-terminus. mGlu5 mutations were generated through site-directed mutagenesis using the Mut Express II Fast Mutagenesis Kit V2 (Vazyme). The successful introduction of the mutations in the polymerase chain reaction products was confirmed through DNA sequencing, with the relevant primer sequences provided in Supplementary Table 2.

HEK293T cells (ATCC; the cells were routinely tested for mycoplasma contamination) were cultured in Dulbecco's modified Eagle's medium (DMEM) supplemented with 10% FBS. All constructs were transfected into cells using the ExFect Transfection Reagent (Vazyme) according to the manufacturer's protocol. To avoid the potential effects of L-glutamine on mGlu5 in classical DMEM, the culture medium was replaced with DMEM GlutaMAX (Gibco) 24 h before transfection. For functional assay, HEK293T cells were plated on 6-cm dishes at a density of 1.2×10^6 cells/dish. After 18–24 h, the cells were transfected at a confluency of 60–80% with 60 ng of wild-type or mutant mGlu5 and 200 ng of EAAT3 (also known as EAAC1). The experiments were performed after incubation for 36 h at 37 °C at 5% CO_2.

Receptor surface expression and IP1 accumulation detection

The receptor surface expression levels were detected by the Nano-Glo® HiBiT Extracellular Detection System (Promega). N-terminal HiBiT-tagged receptors (60 ng/well) were transfected into HEK293T cells seeded in a 12-well plate. After 36 h, the cells were reseeded into white opaque-bottom 96-well plates in Hank's Balanced Salt Solution (HBSS) (15,000 cells in 30 μl/well). Then, 30 μl of assay buffer (Dilute the LgBiT Protein 1:100 and the Nano-Glo® HiBiT Extracellular Substrate 1:50 into an appropriate volume of room temperature Nano-Glo® HiBiT Extracellular) was added to each well and incubated for 10 min. Luminescence counts were determined using the Synergy Neo software (BioTek). The expression level was presented as a percentage relative to that of the wild-type receptor.

IP1 accumulation in HEK293T cells co-transfected with mGlu5 and EAAT3 was measured using an IP-One Gq assay kit (PerkinElmer) according to the manufacturer's instructions. Prior to the assay, glutamate that may have been produced during cell culture was removed. The medium was replaced with 3 ml of glutamate removal buffer (HBSS with 2U/ml Glu-pyruvate transaminase and 250 μM sodium pyruvate, prepared when used). After incubation at 37 °C under 5% CO_2 for 90 min, the cells were reseeded in white opaque-bottom 384-well assay plates (PerkinElmer) at a density of 20,000 cells/well. Briefly, the cells expressing the wild-type mGlu5 or mutants were incubated with increasing concentrations of glutamate at 37 °C for 90 min. After adding the IP1-d2 and anti-IP1 terbium cryptate conjugate reagents, the microplate was incubated in the dark for 1 h at room temperature. The fluorescence signal was measured using a Synergy Neo plate reader (BioTek) with excitation at 330 nm and emission at 620 and 665 nm. The accumulation of IP1 was calculated according to a standard dose–response curve using GraphPad Prism 8.0 (GraphPad software).

Reporting summary

Further information on research design is available in the Nature Portfolio Reporting Summary linked to this article.

Data availability

The associated collective variables of the VFT, CRD, and 7TM, as well as tICA data generated in this study, are included in the Source Data file. Initial structures for MD simulations were obtained from the RCSB PDB database (PDB ID: 6N51, 6N52 and 8TAO). Other GPCRs were also downloaded from the RCSB PDB database at [https://www.rcsb.org/]. NEB calculations and MD simulations were based on AMBER suite, according to [https://ambermd.org/]. The analysis protocol for Markov State Model referred to msmbuilder [http://msmbuilder.org/3.8.0/][79], PyEMMA [http://www.emma-project.org/latest/][80] and Zenodo 13347927[83]. Source data are provided with this paper.

References

1. Hauser, A. S., Attwood, M. M., Rask-Andersen, M., Schioth, H. B. & Gloriam, D. E. Trends in GPCR drug discovery: new agents, targets and indications. *Nat. Rev. Drug Discov.* **16**, 829–842 (2017).

2. Foster, S. R. et al. Discovery of human signaling systems: pairing peptides to G protein-coupled receptors. *Cell* **179**, 895–908.e821 (2019).
3. Pierce, K. L., Premont, R. T. & Lefkowitz, R. J. Seven-transmembrane receptors. *Nat. Rev. Mol. Cell Biol.* **3**, 639–650 (2002).
4. Prezeau, L. et al. Functional crosstalk between GPCRs: with or without oligomerization. *Curr. Opin. Pharmacol.* **10**, 6–13 (2010).
5. Smith, N. J. & Milligan, G. Allostery at G protein-coupled receptor homo- and heteromers: uncharted pharmacological landscapes. *Pharm. Rev.* **62**, 701–725 (2010).
6. Ferre, S. et al. G protein-coupled receptor oligomerization revisited: functional and pharmacological perspectives. *Pharmacol. Rev.* **66**, 413–434 (2014).
7. Liu, X. et al. Unraveling allosteric landscapes of allosterome with ASD. *Nucleic Acids Res.* **48**, D394–D401 (2020).
8. Lu, S. et al. Mechanism of allosteric activation of SIRT6 revealed by the action of rationally designed activators. *Acta Pharm. Sin. B* **11**, 1355–1361 (2021).
9. Pin, J. P., Galvez, T. & Prezeau, L. Evolution, structure, and activation mechanism of family 3/C G-protein-coupled receptors. *Pharm. Ther.* **98**, 325–354 (2003).
10. Niswender, C. M. & Conn, P. J. Metabotropic glutamate receptors: physiology, pharmacology, and disease. *Annu. Rev. Pharm. Toxicol.* **50**, 295–322 (2010).
11. Xue, L. et al. Major ligand-induced rearrangement of the heptahelical domain interface in a GPCR dimer. *Nat. Chem. Biol.* **11**, 134–140 (2015).
12. Koehl, A. et al. Structural insights into the activation of metabotropic glutamate receptors. *Nature* **566**, 79–84 (2019).
13. Wu, H. et al. Structure of a class C GPCR metabotropic glutamate receptor 1 bound to an allosteric modulator. *Science* **344**, 58–64 (2014).
14. Dror, R. O. et al. Activation mechanism of the beta2-adrenergic receptor. *Proc. Natl Acad. Sci. USA* **108**, 18684–18689 (2011).
15. Zhou, Q. et al. Common activation mechanism of class A GPCRs. *Elife* https://doi.org/10.7554/eLife.50279 (2019).
16. Mattedi, G., Acosta-Gutierrez, S., Clark, T. & Gervasio, F. L. A combined activation mechanism for the glucagon receptor. *Proc. Natl Acad. Sci. USA* **117**, 15414–15422 (2020).
17. Suomivuori, C. M. et al. Molecular mechanism of biased signaling in a prototypical G protein-coupled receptor. *Science* **367**, 881–887 (2020).
18. Hauser, A. S. et al. GPCR activation mechanisms across classes and macro/microscales. *Nat. Struct. Mol. Biol.* **28**, 879–888 (2021).
19. Wang, Y. et al. Delineating the activation mechanism and conformational landscape of a class B G protein-coupled receptor glucagon receptor. *Comput. Struct. Biotechnol. J.* **20**, 628–639 (2022).
20. Kunishima, N. et al. Structural basis of glutamate recognition by a dimeric metabotropic glutamate receptor. *Nature* **407**, 971–977 (2000).
21. Kniazeff, J. et al. Closed state of both binding domains of homodimeric mGlu receptors is required for full activity. *Nat. Struct. Mol. Biol.* **11**, 706–713 (2004).
22. Hlavackova, V. et al. Sequential inter- and intrasubunit rearrangements during activation of dimeric metabotropic glutamate receptor 1. *Sci. Signal* **5**, ra59 (2012).
23. Vafabakhsh, R., Levitz, J. & Isacoff, E. Y. Conformational dynamics of a class C G-protein-coupled receptor. *Nature* **524**, 497–501 (2015).
24. Liauw, B. W., Afsari, H. S. & Vafabakhsh, R. Conformational rearrangement during activation of a metabotropic glutamate receptor. *Nat. Chem. Biol.* **17**, 291–297 (2021).
25. Calvo-Tusell, C., Maria-Solano, M. A., Osuna, S. & Feixas, F. Time evolution of the millisecond allosteric activation of imidazole glycerol phosphate synthase. *J. Am. Chem. Soc.* **144**, 7146–7159 (2022).
26. Hollingsworth, S. A. & Dror, R. O. Molecular dynamics simulation for all. *Neuron* **99**, 1129–1143 (2018).
27. Evenseth, L. S. M. et al. Exploring conformational dynamics of the extracellular Venus flytrap domain of the GABA(B) receptor: a path-metadynamics study. *J. Chem. Inf. Model* **60**, 2294–2303 (2020).
28. del Torrent, C. L., Casajuana-Martin, N., Pardo, L., Tresadern, G. & Perez-Benito, L. Mechanisms underlying allosteric molecular switches of metabotropic glutamate receptor 5. *J. Chem. Inf. Model.* **59**, 2456–2466 (2019).
29. Lans, I., Diaz, O., Dalton, J. A. R. & Giraldo, J. Exploring the activation mechanism of the mGlu5 transmembrane domain. *Front Mol. Biosci.* **7**, 38 (2020).
30. Mafi, A., Kim, S. K., Chou, K. C., Guthrie, B. & Goddard, W. A. Predicted structure of fully activated Tas1R3/1R3′ homodimer bound to G protein and natural sugars: structural insights into G protein activation by a class C sweet taste homodimer with natural sugars. *J. Am. Chem. Soc.* **143**, 16824–16838 (2021).
31. Kim, S. K., Chen, Y., Abrol, R., Goddard, W. A. & Guthrie, B. Activation mechanism of the G protein-coupled sweet receptor heterodimer with sweeteners and allosteric agonists. *Proc Natl Acad. Sci. USA* **114**, 2568–2573 (2017).
32. Lei, T. et al. Exploring the activation mechanism of a metabotropic glutamate receptor homodimer via molecular dynamics simulation. *ACS Chem. Neurosci.* **11**, 133–145 (2020).
33. Shukla, D., Meng, Y. L., Roux, B. & Pande, V. S. Activation pathway of Src kinase reveals intermediate states as targets for drug design. *Nat. Commun.* **5**, 3397 (2014).
34. Lu, S. Y. et al. Activation pathway of a G protein-coupled receptor uncovers conformational intermediates as targets for allosteric drug design. *Nat. Commun.* **12**, 4721 (2021).
35. Husic, B. E. & Pande, V. S. Markov state models: from an art to a science. *J. Am. Chem. Soc.* **140**, 2386–2396 (2018).
36. Kohlhoff, K. J. et al. Cloud-based simulations on Google Exacycle reveal ligand modulation of GPCR activation pathways. *Nat. Chem.* https://doi.org/10.1038/Nchem.2272 (2015).
37. Grushevskyi, E. O. et al. Stepwise activation of a class C GPCR begins with millisecond dimer rearrangement. *Proc. Natl Acad. Sci. USA* **116**, 10150–10155 (2019).
38. Manglik, A. et al. Structural insights into the dynamic process of beta2-adrenergic receptor signaling. *Cell* **161**, 1101–1111 (2015).
39. Muto, T., Tsuchiya, D., Morikawa, K. & Jingami, H. Structures of the extracellular regions of the group II/III metabotropic glutamate receptors. *Proc. Natl Acad. Sci. USA* **104**, 3759–3764 (2007).
40. Lecat-Guillet, N. et al. Concerted conformational changes control metabotropic glutamate receptor activity. *Sci. Adv.* **9**, eadf1378 (2023).
41. Wang, X. W. et al. Structural insights into dimerization and activation of the mGlu2-mGlu3 and mGlu2-mGlu4 heterodimers. *Cell Res.* https://doi.org/10.1038/s41422-023-00830-2 (2023).
42. Cannone, G. et al. Conformational diversity in class C GPCR positive allosteric modulation. Preprint at *bioRxiv* https://doi.org/10.1101/2023.11.07.565819 (2023).
43. Krishna Kumar, K. et al. Stepwise activation of a metabotropic glutamate receptor. *Nature* **629**, 951–956 (2024).
44. Olofsson, L. et al. Fine tuning of sub-millisecond conformational dynamics controls metabotropic glutamate receptors agonist efficacy. *Nat. Commun.* **5**, 5206 (2014).
45. Levitz, J. et al. Mechanism of assembly and cooperativity of homomeric and heteromeric metabotropic glutamate receptors. *Neuron* **92**, 143–159 (2016).
46. Naismith, J. H. & Sprang, S. R. Modularity in the TNF-receptor family. *Trends Biochem. Sci.* **23**, 74–79 (1998).

47. Liu, L. et al. Asymmetric activation of dimeric GABA(B) and metabotropic glutamate receptors. *Am. J. Physiol. Cell Physiol.* **325**, C79–C89 (2023).
48. Krishna Kumar, K. et al. Negative allosteric modulation of the glucagon receptor by RAMP2. *Cell* **186**, 1465–1477.e1418 (2023).
49. Lin, S. et al. Structures of G(i)-bound metabotropic glutamate receptors mGlu2 and mGlu4. *Nature* **594**, 583–588 (2021).
50. Seven, A. B. et al. G-protein activation by a metabotropic glutamate receptor. *Nature* **595**, 450–454 (2021).
51. Dore, A. S. et al. Structure of class C GPCR metabotropic glutamate receptor 5 transmembrane domain. *Nature* **511**, 557–562 (2014).
52. Venkatakrishnan, A. J. et al. Molecular signatures of G-protein-coupled receptors. *Nature* **494**, 185–194 (2013).
53. Perez-Benito, L. et al. Molecular switches of allosteric modulation of the metabotropic glutamate 2 receptor. *Structure* **25**, 1153–1162.e1154 (2017).
54. Ling, S. et al. Structural insights into asymmetric activation of the calcium-sensing receptor–Gq complex. *Cell Res.* **34**, 169–172 (2024).
55. Cao, A. M. et al. Allosteric modulators enhance agonist efficacy by increasing the residence time of a GPCR in the active state. *Nat. Commun.* **12**, 5426 (2021).
56. He, F. et al. Allosteric modulation and G-protein selectivity of the Ca^{2+}-sensing receptor. *Nature* **626**, 1141–1148 (2024).
57. Lange, O. F. & Grubmuller, H. Generalized correlation for biomolecular dynamics. *Proteins* **62**, 1053–1061 (2006).
58. Brock, C. et al. Activation of a dimeric metabotropic glutamate receptor by intersubunit rearrangement. *J. Biol. Chem.* **282**, 33000–33008 (2007).
59. Liu, J. K. et al. Allosteric control of an asymmetric transduction in a G protein-coupled receptor heterodimer. *Elife* **6**, ARTN e2698510.7554/eLife.26985 (2017).
60. Dogra, S. & Conn, P. J. Metabotropic glutamate receptors as emerging targets for the treatment of schizophrenia. *Mol. Pharm.* **101**, 275–285 (2022).
61. Stansley, B. J. & Conn, P. J. Neuropharmacological insight from allosteric modulation of mGlu receptors. *Trends Pharm. Sci.* **40**, 240–252 (2019).
62. Gregory, K. J. & Goudet, C. International union of basic and clinical pharmacology. CXI. Pharmacology, signaling, and physiology of metabotropic glutamate receptors. *Pharm. Rev.* **73**, 521–569 (2021).
63. Webb, B. & Sali, A. Comparative protein structure modeling using MODELLER. *Curr. Protoc. Protein Sci.* https://doi.org/10.1002/cpps.20 (2016).
64. Friesner, R. A. et al. Glide: a new approach for rapid, accurate docking and scoring. 1. Method and assessment of docking accuracy. *J. Med. Chem.* **47**, 1739–1749 (2004).
65. Maier, J. A. et al. ff14SB: improving the accuracy of protein side chain and backbone parameters from ff99SB. *J. Chem. Theory Comput.* **11**, 3696–3713 (2015).
66. Salomon-Ferrer, R., Case, D. A. & Walker, R. C. An overview of the Amber biomolecular simulation package. *Wires Comput Mol. Sci.* **3**, 198–210 (2013).
67. Jorgensen, W. L., Chandrasekhar, J., Madura, J. D., Impey, R. W. & Klein, M. L. Comparison of simple potential functions for simulating liquid water. *J. Chem. Phys.* **79**, 926–935 (1983).
68. Ghoreishi, D., Cerutti, D. S., Fallon, Z., Simmerling, C. & Roitberg, A. E. Fast implementation of the nudged elastic band method in AMBER. *J. Chem. Theory Comput.* **15**, 4699–4707 (2019).
69. Henkelman, G. & Jonsson, H. Improved tangent estimate in the nudged elastic band method for finding minimum energy paths and saddle points. *J. Chem. Phys.* **113**, 9978–9985 (2000).
70. Bergonzo, C., Campbell, A. J., Walker, R. C. & Simmerling, C. A partial nudged elastic band implementation for use with large or explicitly solvated systems. *Int. J. Quantum Chem.* **109**, 3781–3790 (2009).
71. Lomize, M. A., Pogozheva, I. D., Joo, H., Mosberg, H. I. & Lomize, A. L. OPM database and PPM web server: resources for positioning of proteins in membranes. *Nucleic Acids Res.* **40**, D370–D376 (2012).
72. Jo, S. et al. CHARMM-GUI 10 years for biomolecular modeling and simulation. *J. Comput. Chem.* **38**, 1114–1124 (2017).
73. Thibado, J. K. et al. Differences in interactions between transmembrane domains tune the activation of metabotropic glutamate receptors. *Elife* https://doi.org/10.7554/eLife.67027 (2021).
74. Darden, T., York, D. & Pedersen, L. Particle mesh Ewald—an N.Log(N) method for Ewald sums in large systems. *J. Chem. Phys.* **98**, 10089–10092 (1993).
75. Ryckaert, J.-P., Ciccotti, G. & Berendsen, H. J. C. Numerical integration of the cartesian equations of motion of a system with constraints: molecular dynamics of n-alkanes. *J. Comput. Phys.* **23**, 327–341 (1977).
76. Noe, F. & Clementi, C. Kinetic distance and kinetic maps from molecular dynamics simulation. *J. Chem. Theory Comput.* **11**, 5002–5011 (2015).
77. Roblitz, S. & Weber, M. Fuzzy spectral clustering by PCCA plus: application to Markov state models and data classification. *Adv. Data Anal. Cl.* **7**, 147–179 (2013).
78. McGibbon, R. T. & Pande, V. S. Variational cross-validation of slow dynamical modes in molecular kinetics. *J. Chem. Phys.* **142**, 124105 (2015).
79. Harrigan, M. P. et al. MSMBuilder: statistical models for biomolecular dynamics. *Biophys. J.* **112**, 10–15 (2017).
80. Scherer, M. K. et al. PyEMMA 2: a software package for estimation, validation, and analysis of Markov models. *J. Chem. Theory Comput.* **11**, 5525–5542 (2015).
81. E, W. & Vanden-Eijnden, E. Towards a theory of transition paths. *J. Stat. Phys.* **123**, 503–523 (2006).
82. McGibbon, R. T. et al. MDTraj: a modern open library for the analysis of molecular dynamics trajectories. *Biophys. J.* **109**, 1528–1532 (2015).
83. Li, M. et al. Delineating the stepwise millisecond allosteric activation mechanism of the class C GPCR dimer mGlu5. *Zenodo* https://doi.org/10.5281/zenodo.13347927 (2024).

Acknowledgements

This study was partly supported by grants from the National Key R&D program of China (No. 2023YFC3404700, to S.L.), the National Natural Science Foundation of China (22077082, to S.L., 81925034, to J.Z.), the Key Research and Development Program of Ningxia Hui Autonomous Region (No. 2022BEG01002, to J.Z.), Innovation Program of Shanghai Municipal Education Commission (2019-01-07-00-01-E00036, to J.Z.), Shanghai Science and Technology Innovation (19431901600, to J.Z.), Zhiyuan Scholar Program (ZIRC2020-06, to M.L.) and Shanghai Jiao Tong University School of Medicine PhD Cultivation Fund for Science and Innovation (24KCPYZD001, to M.L.). The authors acknowledge the Beijing Super Cloud Center (BSCC) for providing HPC resources that have contributed to the research results reported within this paper (http://www.blsc.cn/).

Author contributions

J.Z. and S.L. conceived and supervised the project. J.Z., S.L. and M.L. designed the experiments. M.L. performed the computational experiments and analyzed the data. X. Lan and X.S. performed the biological experiments. M.L. drafted the manuscript, and all authors contributed to specific parts of the manuscript. J.Z. and S.L. assumed responsibility for the manuscript in its entirety. M.L., C.Z., X. Lu and J.P. discussed the results and revised the manuscript.

Competing interests
The authors declare no competing interests.

Additional information
Supplementary information The online version contains supplementary material available at https://doi.org/10.1038/s41467-024-51999-y.

Correspondence and requests for materials should be addressed to Shaoyong Lu or Jian Zhang.

Peer review information *Nature Communications* thanks the anonymous reviewer(s) for their contribution to the peer review of this work. A peer review file is available.

Reprints and permissions information is available at http://www.nature.com/reprints

Publisher's note Springer Nature remains neutral with regard to jurisdictional claims in published maps and institutional affiliations.

Open Access This article is licensed under a Creative Commons Attribution-NonCommercial-NoDerivatives 4.0 International License, which permits any non-commercial use, sharing, distribution and reproduction in any medium or format, as long as you give appropriate credit to the original author(s) and the source, provide a link to the Creative Commons licence, and indicate if you modified the licensed material. You do not have permission under this licence to share adapted material derived from this article or parts of it. The images or other third party material in this article are included in the article's Creative Commons licence, unless indicated otherwise in a credit line to the material. If material is not included in the article's Creative Commons licence and your intended use is not permitted by statutory regulation or exceeds the permitted use, you will need to obtain permission directly from the copyright holder. To view a copy of this licence, visit http://creativecommons.org/licenses/by-nc-nd/4.0/.

© The Author(s) 2024